cubane: i.s. $= 0.47$, 0.47, q.s. $= 0.85$, 1.35; di-iron subsite: i.s. $= 0.08$, q.s. $= 0.87$ mm s^{-1}) measured at 4.2 K. This is concordant with the generally accepted re-assignment of the electronic structure of the six-iron core of the reduced biological cluster as $[\{Fe(I).Fe(I)\}_{subsite}\text{-}\{4Fe4S\}^{2+}_{cubane}]$[29], the established redox configuration of our synthetic cluster. In the synthetic system, we have seen that the reduction of the cubane unit by one electron to the $\{4Fe4S\}^+$ level is easier than is reduction of the $\{Fe(I).Fe(I)\}_{subsite}$, which is coordinatively saturated with a closed-shell (36-electron) configuration. A corresponding state of the H-cluster, in which the cubane unit is reduced to the $\{4Fe4S\}^+$ level, has yet to be detected, although neighbouring $\{4Fe4S\}$ relay centres in *C. pasteurianum* hydrogenase II can be reduced to this level[29]. This raises the question as to whether the $\{4Fe4S\}^+$ level of the H-cluster is physiologically accessed during turnover. A vacant or (weakly) water-coordinated site has been identified crystallographically in the enzyme at the distal iron atom in the resting state of the enzyme. It is possible that protonation at this site lowers the energy of the $Fe(I) \cdot Fe(I)$ subsite unit sufficiently to enable its reduction by the anchored cubane operating at the $\{4Fe4S\}^{2+}$ level. That **D** is capable of electrocatalysing proton reduction may be similarly linked to the formation of a vacant site, in this case by the opening of the μ-S bridge on reduction.

The artificial H-clusters reported here should enhance our understanding of the intimate chemistry of the natural process, and lead to systems with low overpotentials for hydrogen uptake/evolution[11,28]. Given that redox-active $\{4Fe4S\}^{2+}$-centres can be incorporated at high concentration into cysteine functionalized electropolymers[30], we can envisage their modification, using the chemistry we have described, thereby providing a route to advanced electrode materials. □

1. Peters, J. W., Lanzilotta, W. N., Lemon, B. J. & Seefeldt, L. C. X-ray crystal structure of the Fe-only hydrogenase (Cpl) from *Clostridium pasteurianum* to 1.8 angstrom resolution. *Science* **282**, 1853–1858 (1998).

2. Nicolet, Y., Piras, C., Legrand, P., Hatchikian, C. E. & Fontecilla-Camps, J. C. *Desulfovibrio desulfuricans* iron hydrogenase: the structure shows unusual coordination to an active site Fe binuclear center. *Struct. Fold. Des.* **7**, 13–23 (1999).

3. Nicolet, Y., Lemon, B. J., Fontecilla-Camps, J. C. & Peters, J. W. A novel FeS cluster in Fe-only hydrogenases. *Trends Biochem. Sci.* **25**, 138–143 (2000).

4. Armstrong, F. A. Hydrogenases: active site puzzles and progress. *Curr. Opin. Chem. Biol.* **8**, 133–140 (2004).

5. Evans, D. J. & Pickett, C. J. Chemistry and the hydrogenases. *Chem. Soc. Rev.* **32**, 268–275 (2003).

6. Lyon, E. J., Georgakaki, I. P., Reibenspies, J. H. & Darensbourg, M. Y. Carbon monoxide and cyanide ligands in a classical organometallic complex model for Fe-only hydrogenase. *Angew. Chem. Int. Edn* **38**, 3178–3180 (1999).

7. Schmidt, M., Contakes, S. M. & Rauchfuss, T. B. First generation analogues of the binuclear site in the Fe-only hydrogenases: $Fe_2(\mu\text{-}SR)_2(CO)_4(CN)_2^{2-}$. *J. Am. Chem. Soc.* **121**, 9736–9737 (1999).

8. Le Cloirec, A. *et al.* A di-iron dithiolate possessing structural elements of the carbonyl/cyanide sub-site of the H-centre of Fe-only hydrogenase. *Chem. Commun.* 2285–2286 (1999).

9. Razavet, M. *et al.* Transient FTIR spectroelectrochemical and stopped-flow detection of a mixed valence {Fe(I)-Fe(II)} bridging carbonyl intermediate with structural elements and spectroscopic characteristics of the di-iron sub-site of all-iron hydrogenase. *Chem. Commun.* 700–701 (2002).

10. George, S. J., Cui, Z., Razavet, M. & Pickett, C. J. The di-iron subsite of all-iron hydrogenase: Mechanism of cyanation of a synthetic {2Fe3S} – carbonyl assembly. *Chem. Eur. J.* **8**, 4037–4046 (2002).

11. Gloaguen, F., Lawrence, J. D., Rauchfuss, T. B., Benard, M. & Rohmer, M. M. Bimetallic carbonyl thiolates as functional models for Fe-only hydrogenase. *Inorg. Chem.* **41**, 6573–6582 (2002).

12. Ott, S., Kritikos, M., Akermark, B., Sun, L. C. & Lomoth, R. A biomimetic pathway for hydrogen evolution from a model of the iron hydrogenase active site. *Angew. Chem. Int. Edn* **43**, 1006–1009 (2004).

13. Cao, Z. X. & Hall, M. B. Modeling the active sites in metalloenzymes. 3. Density functional calculations on models for Fe-hydrogenase: Structures and vibrational frequencies of the observed redox forms and the reaction mechanism at the diiron active center. *J. Am. Chem. Soc.* **123**, 3734–3742 (2001).

14. Liu, Z. P. & Hu, P. A density functional theory study on the active center of Fe-only hydrogenase: Characterization and electronic structure of the redox states. *J. Am. Chem. Soc.* **124**, 5175–5182 (2002).

15. Bruschi, M., Fantucci, P. & De Gioia, L. Density functional theory investigation of the active site of Fe-hydrogenases. Systematic study of the effects of redox state and ligands hardness on structural and electronic properties of complexes related to the $[2Fe]_H$ subcluster. *Inorg. Chem.* **43**, 3733–3741 (2004).

16. *Basic Research Needs for the Hydrogen Economy* (Report of the Basic Energy Sciences Workshop on Hydrogen Production, Storage, and Use, 13–15 May 2003, Office of Science, US Department of Energy); available at ⟨http://www.eere.energy.gov/hydrogenandfuelcells/pdfs/bes_project.pdf⟩.

17. *Platinum and Hydrogen for Fuel Cell Vehicles* (UK Department for Transport, September 2003); available at ⟨http://www.dft.gov.uk/stellent/groups/dft_roads/documents/page/dft_roads_024056.hcsp⟩.

18. Reihlen, H., Gruhl, A. & Hessling, G. Über den photochemischen und oxydativen Abbau von Carbonylen. *Liebigs Ann. Chem.* **472**, 268–287 (1929).

19. Razavet, M. *et al.* All-iron hydrogenase: synthesis, structure and properties of {2Fe3S}-assemblies related to the di-iron sub-site of the H-cluster. *Dalton Trans.* 586–595 (2003).

20. Stack, T. D. P. & Holm, R. H. Subsite-specific functionalization of the $[4Fe\text{-}4S]^{2+}$ analog of iron sulfur protein clusters. *J. Am. Chem. Soc.* **109**, 2546–2547 (1987).

21. Perdew, J. P. Density-functional approximation for the correlation-energy of the inhomogeneous electron-gas. *Phys. Rev. B* **33**, 8822–8824 (1986).

22. Becke, A. D. Density-functional exchange-energy approximation with correct asymptotic-behavior. *Phys. Rev. A* **38**, 3098–3100 (1988).

23. Schafer, A., Huber, C. & Ahlrichs, R. Fully optimized contracted Gaussian-basis sets of triple zeta valence quality for atoms Li to Kr. *J. Chem. Phys.* **100**, 5829–5835 (1994).

24. Wang, L. S., Ding, C. F., Wang, X. B. & Barlow, S. E. Photodetachment photoelectron spectroscopy of multiply charged anions using electrospray ionization. *Rev. Sci. Instrum.* **70**, 1957–1966 (1999).

25. Yang, X., Razavet, M., Wang, X. B., Pickett, C. J. & Wang, L. S. Probing the electronic structure of the di-iron subsite of Fe-hydrogenase: A photoelectron spectroscopic study of Fe(I)-Fe(I) model complexes. *J. Phys. Chem. A* **107**, 4612–4618 (2003).

26. Wang, X. B. *et al.* Probing the intrinsic electronic structure of the cubane [4Fe4S] cluster: Nature's favorite cluster for electron transfer and storage. *J. Am. Chem. Soc.* **125**, 14072–14081 (2003).

27. Zhao, X. *et al.* Catalysis of H_2/D_2 scrambling and other H/D exchange processes by [Fe]-hydrogenase model complexes. *Inorg. Chem.* **41**, 3917–3928 (2002).

28. Tard, C., Liu, X., Hughes, D. L. & Pickett, C. J. A novel $\{Fe^I\text{-}Fe^{II}\text{-}Fe^{II}\text{-}Fe^I\}$ iron thiolate carbonyl assembly which electrocatalyses hydrogen evolution. *Chem. Commun.* 133–135 (2005).

29. Popescu, C. V. & Munck, E. Electronic structure of the H cluster in Fe-hydrogenases. *J. Am. Chem. Soc.* **121**, 7877–7884 (1999).

30. Pickett, C. J. & Ryder, K. S. Bioinorganic reaction centers on electrodes — Modified electrodes possessing amino-acid, peptide and ferredoxin-type groups on a poly(pyrrole) backbone. *J. Chem. Soc. Dalton Trans.* 2181–2189 (1994).

Supplementary Information accompanies the paper on **www.nature.com/nature**.

Highly variable Northern Hemisphere temperatures reconstructed from low- and high-resolution proxy data

Anders Moberg[1], Dmitry M. Sonechkin[2], Karin Holmgren[3], Nina M. Datsenko[2] & Wibjörn Karlén[3]

[1]*Department of Meteorology, Stockholm University, SE-106 91 Stockholm, Sweden*
[2]*Dynamical-Stochastical Laboratory, Hydrometeorological Research Centre of Russia, Bolshoy Predtechensky Lane 11/13, Moscow 123 242, Russia*
[3]*Department of Physical Geography and Quaternary Geology, Stockholm University, SE-106 91 Stockholm, Sweden*

A number of reconstructions of millennial-scale climate variability have been carried out in order to understand patterns of natural climate variability, on decade to century timescales, and the role of anthropogenic forcing[1–8]. These reconstructions have mainly used tree-ring data and other data sets of annual to decadal resolution. Lake and ocean sediments have a lower time resolution, but provide climate information at multicentennial timescales that may not be captured by tree-ring data[9,10]. Here we reconstruct Northern Hemisphere temperatures for the past 2,000 years by combining low-resolution proxies with

tree-ring data, using a wavelet transform technique[11] to achieve timescale-dependent processing of the data. Our reconstruction shows larger multicentennial variability than most previous multi-proxy reconstructions[1–4,7], but agrees well with temperatures reconstructed from borehole measurements[12] and with temperatures obtained with a general circulation model[13,14]. According to our reconstruction, high temperatures—similar to those observed in the twentieth century before 1990—occurred around AD 1000 to 1100, and minimum temperatures that are about 0.7 K below the average of 1961–90 occurred around AD 1600. This large natural variability in the past suggests an important role of natural multicentennial variability that is likely to continue.

Global temperatures are currently rising, and future scenarios suggest large changes in precipitation patterns and temperatures[15]. Reconstructing past climate is essential for enhanced understanding of climate variability, and provides necessary background knowledge for improving predictions of future changes. From multi-proxy combinations[1–4,7] of climate proxy data (for example, from tree rings, corals and ice cores), or from reconstructions based solely on tree-ring data[5–6,16], past surface temperatures have been inferred by calibration to instrumental temperature data using statistical relationships. Past surface temperature changes have also been inferred from temperature profiles along deep terrestrial boreholes[12], where physical laws rather than statistical relations are used to estimate temperature trends. Borehole measurements[12] and some reconstructions based on tree-ring data[6,16] indicate a larger warming trend in the past 500 yr than do multi-proxy reconstructions[1–4,7].

Although differences in the amplitude of centennial temperature variability have been discussed in the literature[8,15], the picture with relatively small variability (shown by multi-proxy reconstructions[1–4,7]) is arguably best known by a wider audience. One reason for this is the prominent role that the multi-proxy reconstruction by Mann *et al.*[1,2] had in the latest IPCC report[15] and in public media. Recent findings[14], however, suggest that considerable underestimation of centennial Northern Hemisphere temperature variability may result when regression-based methods, like those used by Mann *et al.*[1,2], are applied to noisy proxy data with insufficient spatial representativity. It is thus important to explore other techniques and other data types, and also to use data from more regions than previously examined.

A view has been expressed that only tree-ring and other high-resolution data are useful for quantitative large-scale temperature reconstructions[3,8]. Tree-ring data, however, have a well-documented difficulty in reliably reproducing multicentennial temperature variability[17]. Special standardization techniques for extracting multicentennial information exist[6,16], but they do not ensure an accurate reconstruction[10]. Natural archives with lower temporal resolution (often various sediments) have potential for providing climate information at multicentennial timescales that may not be captured by tree-ring data[9]. Low-resolution data, on the other hand, can sometimes have dating errors of up to more than 100 yr (ref. 9). Such errors are intolerable at interannual to multidecadal timescales[8], but if these data are used only for longer timescales the errors become relatively small in relation to the timescales of interest.

Our aim is to combine low-frequency climate information (contained in low-resolution proxy data) with high-frequency information (from tree-ring data) in order to derive a 2,000-yr-long Northern Hemisphere temperature reconstruction in which we avoid using each proxy type at timescales where it is most unreliable, but instead use it only where it has its greatest advantages. To achieve this, we developed a method that allows a timescale-dependent data decomposition by application of a wavelet transform[11] technique.

The number of available 2,000-yr-long local-to-regional scale temperature proxy series is very limited[8]. We found seven tree-ring series and eleven low-resolution proxy series. For the period before AD 1400, this number is similar to previous reconstructions[1–7]. Among the eleven low-resolution series were nine already calibrated to local/regional temperatures for different Northern Hemisphere regions, whereas two were only available in original proxy data units. The data set includes climatic information from the North American and Eurasian continents and from the Atlantic and Indian oceans (Fig. 1, Table 1; see Supplementary Information for further details and references).

Various averages (see Methods) of the nine already calibrated low-resolution series (Table 1, site numbers 2–10) depict, when low-pass filtered to highlight multicentennial variability (Fig. 2a), a temperature maximum in the ninth or tenth centuries and a minimum in the sixteenth century, with a total range of 0.6 to 0.9 K. This is a substantially larger multicentennial temperature range compared to previous multi-proxy reconstructions[1–4,7], exemplified in Fig. 2a with the Northern Hemisphere reconstruction by Mann and Jones[7]. The conflicting views provided by the low-resolution series and this reconstruction illustrate a clear need for further research to determine the size of natural low-frequency climate variability.

Simple averages of temperature proxy series, such as those shown in Fig. 2a, can yield adequate estimates of Northern Hemisphere century-scale mean-temperature anomalies[14]. But to obtain a reconstruction covering a complete range of timescales we created a wavelet transform[11], supposed to be approximately representative for the Northern Hemisphere (Fig. 2e), such that only information from the tree-ring records contributes to timescales less than 80 yr and all eleven low-resolution proxies contribute only to the longer timescales (see Methods for details). From the wavelet transform, which was calculated using standardized (that is, unitless) proxy series, a dimensionless reconstruction was obtained by calculating the inverse wavelet transform[11]. Given the small number of tree-ring series, their contribution is best thought of as an approximation of the statistical character of variability at <80-yr scales. A sample size of eleven low-resolution series is reasonable for reconstructing >80-yr variability, given that the number of spatial degrees of freedom on the entire globe is about five at centennial time-
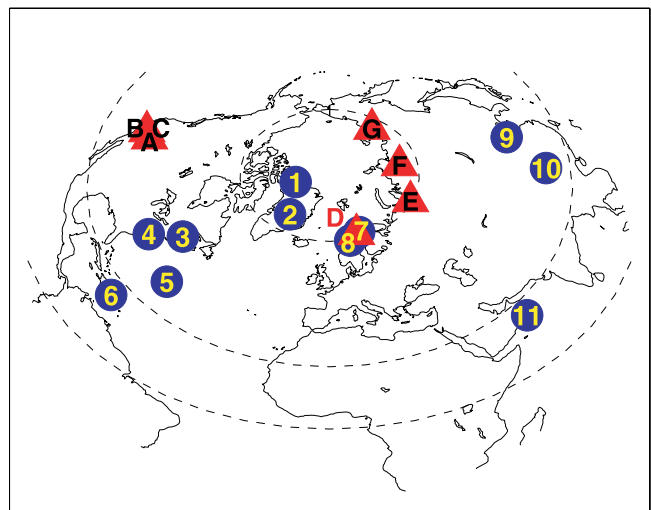

Figure 1 Locations of proxy data sites. Shown are the locations of eleven low-resolution proxy records (blue circles, numerals 1–11, see Table 1 for site details) and seven tree-ring series (red triangles, letters A–G). Dashed latitude lines indicate the Equator, the Tropic of Cancer and the Arctic Circle. See Supplementary Information for further details and references.

scales[18]. The contribution from each low-resolution proxy series to the total variance at >80-yr scales in the Northern Hemisphere reconstruction is given in Table 1.

To calibrate the reconstruction, its mean value and variance were adjusted to agree with the instrumental record of Northern Hemisphere annual mean temperatures[19] in the overlapping period AD 1856–1979 (Fig. 2b). This technique avoids the problem with underestimation of low-frequency variability associated with regression-based calibration methods[14]. Jack-knifed estimates (light-blue curves in Fig. 2b) of the low-frequency component (>80-yr scales, dark blue), where each of the eleven low-resolution proxies are excluded one at a time, are all very similar, demonstrating that the reconstruction is robust to the omission of any single low-resolution proxy series.

The reconstruction depicts two warm peaks around AD 1000 and 1100 and pronounced coolness in the sixteenth and seventeenth centuries, with an overall temperature range for the low-frequency component (>80-yr scales) of about 0.65 K. This amplitude can be compared with that in the smoothed and averaged low-resolution series in Fig. 2a, where the data used had been calibrated to temperatures by their original investigators. The size of the overall amplitudes of the series in Fig. 2a (0.6–0.9 K) and Fig. 2b (0.65 K, blue curve) indicates that the reconstructed multicentennial variability in Fig. 2b has not been inflated by the standardization, the wavelet processing and the subsequent calibration technique. The peaks in medieval times are at the same level as much of the twentieth century, although the post-1990 warmth seen in the instrumental data (green curve in Fig. 2b) appears to be unprecedented.

Changes in radiative forcing due to variability in solar irradiance, the amount of aerosols from volcanic eruptions and greenhouse gas concentrations have been important agents causing climatic variability in the past millennium[1,8,20–25]. Reconstructions of the temporal evolution of these variables have been used to drive climate models, ranging from simple energy balance models to fully coupled atmosphere–ocean general circulation models[8,13,14,20,22,23,25]. The Northern Hemisphere temperature series obtained from such an experiment with the coupled model ECHO-G[13,14,25,26] for the AD 1000–1990 period (Fig. 2c) is qualitatively remarkably similar to our multi-proxy reconstruction, although the model shows a somewhat larger variability. Particularly strong qualitative similarity is seen at timescales longer than centennial (compare the two wavelet transform patterns, Fig. 2e, f), but some high-frequency details are also in good agreement (for example, the double peaks around AD 1000 and 1100, and two short cooling periods at AD 1460 and 1820). The model's variability before the twentieth century is largely determined by the combined effects of the reconstructed solar and volcanic forcing (that is, natural forcing) that was used in the integration[13,25], whereas the notably strong warming in the model data after AD 1900 is largely due to rapidly increasing concentrations of anthropogenic greenhouse gases[13,25,27]. The similarity between our reconstruction and the ECHO-G model series supports the case of a rather pronounced hemispheric low-frequency temperature variability resulting from the climate system's response to natural

Table 1 Summary information for low-resolution proxy series

No.*	Site†	Proxy type and interpretation‡	Dating type (max. dating error)	First, last year AD#	Sample resolution (no. of samples)§	Variance fraction (%) in >80-yr scales	
						Proxy‖	NH¶
1	Agassiz Ice Cap, Ellesmere Island, Canada, 81° N, 73° W	Ice melt, layer stratigraphy, summer T	Annual layer, theoretical model, ash layers (±10%)	−9, 1961	5 (393)	2.4	0.3
2	GRIP borehole, Greenland, 73° N, 38° W	Borehole T, annual T	Theoretical model	−300, 1996	50 (40)	89.2	12.5
3	Conroy Lake, Eastern US, 46° N, 68° W	Pollen, lake sediments, summer T	Annual laminations	35, 1968	7–40 (68)	69.2	9.7
4	Chesapeake Bay, Eastern US, 38° N, 76° W	Shells, Mg/Ca variation, spring T	^{14}C (±160 yr), ^{210}Pb and ^{137}Cs	5, 1995	1–65 (427)	30.8	4.3
5	N. Sargasso Sea, 33° N, 57° W	Foraminifera, δ^{18}O, annual SST	^{14}C (±160 yr)	−300, 1925	50–150 (30)	65.0	9.1
6	NE Caribbean Sea, 18° N, 67° W	Foraminifera, δ^{18}O, annual SST	^{14}C (±200 yr)	133, 1950	30–160 (26)	99.6	14.0
7	Lake Tsuolbmajavri, N. Finland, 68° N, 22° E	Diatoms, lake sediments, summer T	^{14}C (± 169 yr)	−300, 1950	~70 (29)	61.5	9.9
8	Søylegrotta Cave, Mo i Rana, N. Norway, 66° N, 13° E	Stalagmite, δ^{18}O, annual T	^{230}Th/^{234}U (±46 yr)	−300, 1938	~20 (103)	47.3	7.6
9	Shihua Cave, Beijing, China, 40° N, 116° E	Stalagmite, layer thickness, summer T	Layer counting (±5 yr)	−300, 1985	1 (1985)	32.2	5.2
10	China, 20–42° N, 80–130° E	Composite of 9 records, annual T	Layer counting, ^{14}C (±200 yr)	0, 1990	10 (200)	89.8	14.5
11	Arabian Sea, 18° N, 58° E	% *Globigerina bulloides*, up-welling, monsoons, summer and winter T	^{14}C (±100 yr)	−300, 1986	15–180 (63)	78.6	12.7

*Numbered as in Fig. 1.
†References and further site details are given in Supplementary Information.
‡T, temperature; SST, sea surface temperature.
#Negative numbers mean years before AD 1.
§Sample resolution in years. Number of samples after year AD 1 given in parentheses.
‖For each proxy, the fraction of its total variance that occurs in its >80-yr scales (wavelet scales 10–22, see Methods) is listed.
¶For each proxy, its contribution (in %) to the total variance in the low-frequency component (wavelet scales 10–22) of the Northern Hemisphere (NH) temperature reconstruction is listed. These contributions are determined by the values in the second to last column. The resulting contributions by data from different regions are geographically well distributed; Arctic 12.9, Eastern US 14.0, Fennoscandia 17.6, China 19.7, Oceans 35.8. Furthermore, the five proxies that are annual mean temperature indicators (nos 2, 5, 6, 8, 10) together contribute 57.8% of the variance in the low-frequency component of the NH reconstruction.

changes in radiative forcing.

As in all palaeoclimate reconstructions, there are uncertainties in this one. Efforts to quantify uncertainties in the low-frequency component are illustrated with blue bands of different colours in Fig. 2d. Accounting for the total uncertainty, the cooling from the maxima around AD 1000 and 1100 to the minimum near AD 1600 is between 0.3 K and 1.1 K for the >80-yr component. Only the smallest value is similar to the corresponding temperature change in previous multi-proxy reconstructions[1–4,7]. (Compare with the reconstruction of Mann et al.[1,2], which is also shown in Fig. 2d (orange curve, yellow uncertainty range) after smoothing to show >80-yr variability.) In contrast, the warming trend depicted by our reconstruction in the past 500 yr is entirely consistent with estimates of Northern Hemisphere ground surface temperature (GST) trends from temperature measurements in nearly 700 boreholes[12]. Although trends at individual borehole sites are very noisy, hemispheric mean GST trends are robust to different aggregation and weighting schemes[12] (illustrated by the two brown curves in Fig. 2d), and show a warming of ~1 K during the interval AD 1500–2000, of which about half fell in the twentieth century.

There are several reasons for the notable differences between our and previous multi-proxy reconstructions. The reconstruction of Mann and Jones[7] has a large amount of data in common with ours, but these workers combined tree-ring data with decadally resolved proxies without any separate treatment at different timescales. Furthermore, our data set contains some centennially resolved data from the oceans, while Mann and Jones used only annually to decadally resolved data from continents or from locations very near the coast. Different calibration methods (regression in the work of Mann and Jones versus variance scaling in this study) are another reason. Possible explanations for the small low-frequency variability in the multi-proxy reconstruction of Mann et al.[1,2] have recently been discussed in detail elsewhere[14].

Our multi-proxy reconstruction achieves a relatively large multi-centennial variability by separately considering the information in tree-ring data and low-resolution proxy records. Much more effort, however, is needed to develop new proxy data series and to determine how proxy data should best be chosen, combined and calibrated. The wavelet approach allows for separate weighting of proxies at different timescales. A goal for further research could be to determine how such weighting should be undertaken, while simultaneously taking spatial representativity into account. New experiments with distorted 'pseudoproxy' data[14,28,29] from forced general circulation model runs, using various types of distortions,
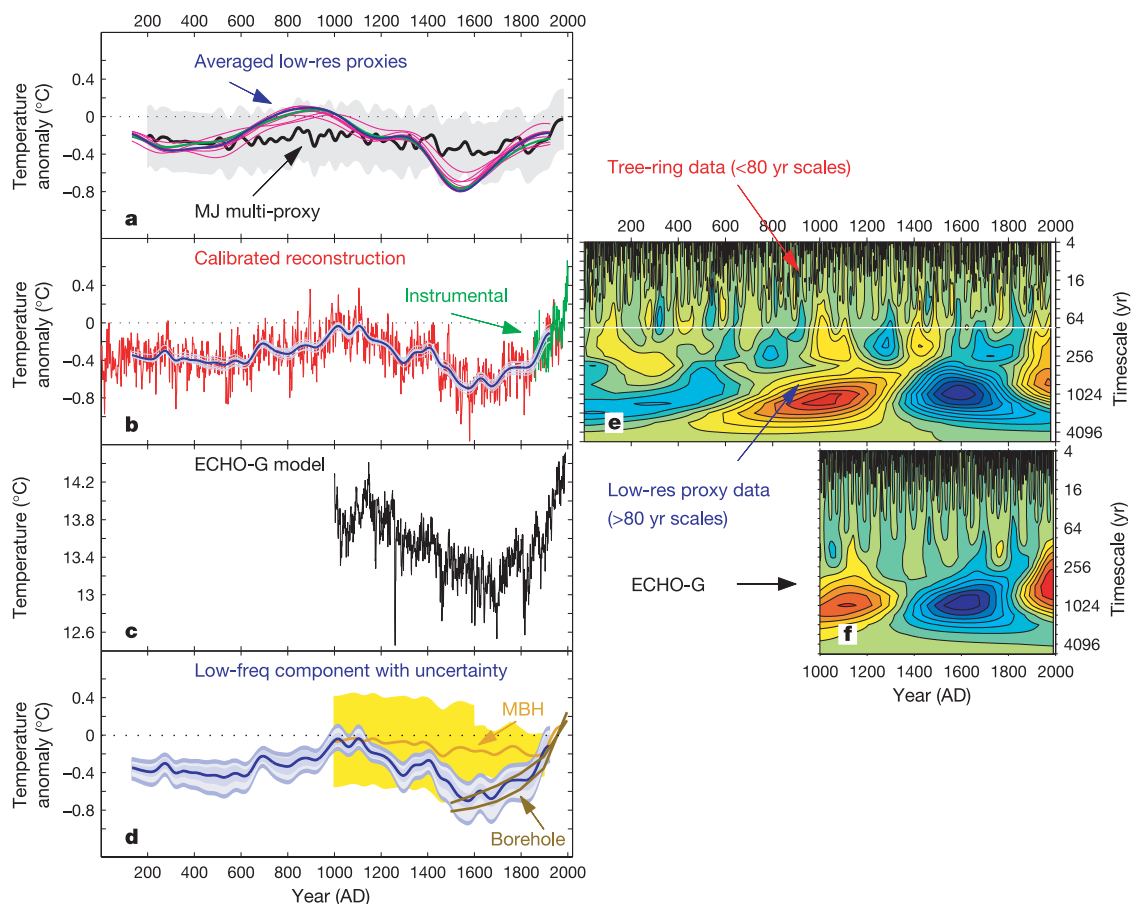

Figure 2 Estimations of Northern Hemisphere mean temperature variations. **a**, Previous multi-proxy reconstruction (MJ: from Mann and Jones[7], black line) with ±2 s.d. uncertainty (grey shading), and various averages (blue, green, magenta; see Methods) of smoothed low-resolution temperature indicators (nos 2–10 in Table 1). **b**, Our multi-proxy reconstruction AD 1–1979 (red) with its >80-yr component AD 133–1925 (blue) and its jack-knifed estimates (light blue), and the instrumental record[19] (green). **c**, Forced ECHO-G model[13,14,26]. **d**, Low-frequency component of multi-proxy reconstruction in **b** (blue curve) with confidence intervals for three separate uncertainties. The innermost medium-blue band shows the uncertainty due to variance among the low-resolution proxy series. The two outer bands show the uncertainty in the variance scaling factor (light blue) and the constant adjustment (outermost blue band) separately. Each uncertainty is illustrated with an approximate 95% confidence interval (see Supplementary Information). Also shown are ground surface temperatures estimated from boreholes[12] with their uncertainty interval (brown; see Methods), and the >80-yr component of a previous multi-proxy reconstruction (MBH: from Mann et al.[1,2], orange) with ±2 s.d. uncertainty (yellow). **e**, **f**, Wavelet transform (see Methods) of the series in **b** and **c** where warm/cold anomalies are red/blue. Temperature anomalies in **a**, **b** and **d** are with respect to the 1961–90 average.

should be useful in this context.

We find no evidence for any earlier periods in the last two millennia with warmer conditions than the post-1990 period—in agreement with previous similar studies[1–4,7]. The main implication of our study, however, is that natural multicentennial climate variability may be larger than commonly thought, and that much of this variability could result from a response to natural changes in radiative forcings. This does not imply that the global warming in the last few decades[15,19] has been caused by natural forcing factors alone, as model experiments that use natural-only forcings fail to reproduce this warming[15,23,27,30]. Nevertheless, our findings underscore a need to improve scenarios for future climate change by also including forced natural variability—which could either amplify or attenuate anthropogenic climate change significantly. □

Methods

Wavelet transformation

The wavelet transform[11] (WT) decomposes a time series into time–frequency space, enabling the identification of both the dominant modes of variability and how those modes vary with time. We used the Mexican hat[11] wavelet, after linear interpolation to annual resolution, to decompose each proxy series into 22 wavelet 'voices'. These are 22 separate time series, where each depict the variability in the original series at each of the timescales near the Fourier periods 4, $4\sqrt{2}$, 8, $8\sqrt{2}$, …, $4,096\sqrt{2}$ yr. This ranges from the smallest possible scale for the Mexican hat wavelet up to a few times the length of the 2,000-yr-long time interval of interest. Before calculating the WT, padding with surrogate data to extend the proxy series from their last value to the year AD 2300 was applied to limit boundary effects at the longest timescales. As padding data we used the mean value for the last 50 yr with data in each series. For those records that do not have data back at least to 300 BC, similar padding was also made at the beginning of records.

Averaging of calibrated low-resolution temperature indicators

Nine low-resolution proxy series (Table 1) are available as calibrated local/regional temperature indicators (numbers 2–10). Five are annual mean (nos 2, 5, 6, 8, 10), one is a spring (no. 4) and three are summer (nos 3, 7, 9) temperature indicators. Multicentennial variability (highlighting >340-yr scales) in these series was extracted by first applying the WT to each series and then the inverse WT only for wavelet voices 14–22. Timescales of >340 yr are long enough to ensure that only information at frequencies lower than the Nyquist frequency for the most poorly resolved proxy series are used. Figure 2a shows arithmetic (green) and cos-latitude weighted (blue) averages of all nine indicators. Jack-knifed estimates of the cos-latitude weighted averages, where each of the nine indicators were removed one at a time, are also shown (magenta). These series are plotted in Fig. 2a for the period AD 133–1925 (when all have data) such that their mean values agree with the Mann and Jones reconstruction[7] in the interval AD 200–1925. Minor differences between the arithmetic and cos-latitude weighted series indicate robustness to weighting choice. The similarity among the jack-knifed estimates indicates that the overall temperature range is relatively little affected by the removal of any individual indicator.

Timescale-dependent reconstruction

The multi-proxy reconstruction in Fig. 2b was constructed as follows. First, the data set of 19 proxy series in Fig. 1 was divided into two half-hemispheric subsets (western and eastern half). After wavelet transformation of each individual proxy series into 22 voices as described above (here using standardized series obtained by subtracting the mean and dividing by the standard deviation, after linear interpolation to annual resolution), a scale-by-scale averaging of wavelet voices was undertaken. For each wavelet scale from 1 to 9 (Fourier timescales <80 yr), the voices from the individual tree-ring series were averaged and, similarly, for each wavelet scale from 10 to 22 (Fourier timescales >80 yr) the corresponding voices from the individual low-resolution proxy series were averaged. Merging of the tree-ring-data average voices 1–9 with the low-resolution-data average voices 10–22 gave one complete WT with voices 1–22 for each half-hemispheric subset. The average of these two WTs then gave the whole-hemispheric WT shown in Fig. 2e. The rationale for dividing into half-hemispheric subsets is similar to that used in gridding; namely, to ensure that regions with many data series are weighted the same as regions (of the same size) with few data series. However, for our data set, little difference would be obtained if all data were placed in one whole-hemispheric set. A dimensionless Northern Hemisphere temperature reconstruction was obtained by calculating the inverse transform. Finally, this time series was calibrated by adjusting its variance and mean value to be the same as in the instrumental data[19] in the overlapping period AD 1856–1979 (Fig. 2b). Separate estimates of uncertainties due to variance among individual low-resolution proxy data and in the determination of the variance scaling factor and constant adjustment term are explained in Supplementary Information.

Plotting GST trends

The two curves for GST trends[12] shown in Fig. 2d correspond to the upper and lower bounds for different area- and occupancy-weighted GST reconstructions, as illustrated in figure 3 of ref. 12. To help visual comparison with our multi-proxy reconstruction, the GST trends are plotted with reference to the AD 1961–90 average in Fig. 2d. This was achieved by shifting the GST trend-curves such that they cross the zero level at 1958.5, which is the time when the twentieth century linear trend of the Northern Hemisphere instrumental surface air temperature[19] (anomalies with respect to AD 1961–90) crosses the zero level. (The same technique was used in figure 5 of ref. 12.)

1. Mann, M. E., Bradley, R. S. & Hughes, M. K. Global-scale temperature patterns and climate forcing over the past six centuries. *Nature* **392,** 779–787 (1998).
2. Mann, M. E., Bradley, R. S. & Hughes, M. K. Northern hemisphere temperatures during the past millennium: Inferences, uncertainties, and limitations. *Geophys. Res. Lett.* **26,** 759–762 (1999).
3. Jones, P. D., Briffa, K. R., Barnett, T. P. & Tett, S. F. B. High-resolution palaeoclimatic records for the last millennium: interpretation, integration and comparison with General Circulation Model control-run temperatures. *Holocene* **8,** 455–471 (1998).
4. Crowley, T. J. & Lowery, T. S. How warm was the Medieval warm period? *Ambio* **29,** 51–54 (2000).
5. Briffa, K. R. Annual climate variability in the Holocene: interpreting the message of ancient trees. *Quat. Sci. Rev.* **19,** 87–105 (2000).
6. Esper, J., Cook, E. R. & Schweingruber, F. H. Low-frequency signals in long tree-ring chronologies for reconstructing past temperature variability. *Science* **295,** 2250–2253 (2002).
7. Mann, M. E. & Jones, P. D. Global surface temperatures over the past two millennia. *Geophys. Res. Lett.* **30,** 1820, doi:10.1029/2003GL017814 (2003).
8. Jones, P. D. & Mann, M. E. Climate over past millennia. *Rev. Geophys.* **42,** doi:10.1029/2003RG000143 (2004).
9. Bradley, R. S. *Paleoclimatology: Reconstructing Climates of the Quaternary* (Academic, San Diego, 1999).
10. Esper, J., Frank, D. C. & Wilson, R. J. S. Climate reconstructions: Low-frequency ambition and high-frequency ratification. *Eos* **85,** 113 (2004).
11. Mallat, S. *A Wavelet Tour of Signal Processing* (Academic, San Diego, 1999).
12. Pollack, H. N. & Smerdon, J. E. Borehole climate reconstructions: Spatial structure and hemispheric averages. *J. Geophys. Res.* **109,** doi:10.1029/2003JD004163 (2004).
13. González-Rouco, F., von Storch, H. & Zorita, E. Deep soil temperature as a proxy for surface air-temperature in a coupled model simulation of the last thousand years. *Geophys. Res. Lett.* **30,** 2116, doi:10.1029/2003GL018264 (2003).
14. von Storch, H. *et al.* Reconstructing past climate from noisy proxy data. *Science* **306,** 679–682 (2004).
15. Intergovernmental Panel on Climate Change. *Climate Change 2001: The Scientific Basis* (IPCC, Geneva, 2001).
16. Briffa, K. R. *et al.* Low-frequency temperature variations from a northern tree ring density network. *J. Geophys. Res.* **106,** 2929–2941 (2001).
17. Cook, E. R., Briffa, K. R., Meko, D. M., Graybill, D. A. & Funkhouser, G. The 'segment length curse' in long tree-ring chronology development for palaeoclimatic studies. *Holocene* **5,** 229–237 (1995).
18. Jones, P. D., Osborn, T. J. & Briffa, K. R. Estimating sampling errors in large-scale temperature averages. *J. Clim.* **10,** 2548–2568 (1997).
19. Jones, P. D. & Moberg, A. Hemispheric and large-scale surface air temperature variations: An extensive revision and an update to 2001. *J. Clim.* **16,** 206–223 (2003).
20. Crowley, T. J. Causes of climate change over the past 1000 years. *Science* **289,** 270–277 (2000).
21. Shindell, D. T., Schmidt, G. A., Mann, M. E., Rind, D. & Waple, A. Solar forcing of regional climate change during the Maunder Minimum. *Science* **294,** 2149–2152 (2001).
22. Bauer, E., Claussen, M., Brovkin, V. & Huenerbein, A. Assessing climate forcings of the Earth system for the past millennium. *Geophys. Res. Lett.* **30,** 1276, doi:10.1029/2002GL016639 (2003).
23. Bertrand, C., Loutre, M.-F., Crucifix, M. & Berger, A. Climate of the last millennium: a sensitivity study. *Tellus A* **54,** 221–244 (2002).
24. Shindell, D. T., Schmidt, G. A., Miller, R. L. & Mann, M. E. Volcanic and solar forcing of climate change during the Maunder Minimum. *J. Clim.* **16,** 4094–4107 (2003).
25. Zorita, E. *et al.* Climate evolution in the last five centuries simulated by an atmosphere-ocean model: global temperatures, the North Atlantic Oscillation and the Late Maunder Minimum. *Meteorol. Z.* **13,** 271–289 (2004).
26. Legutke, S. & Voss, R. *The Hamburg Atmosphere-Ocean Coupled Circulation Model ECHO-G* (Technical Report 18, Deutsches Klimarechenzentrum, Hamburg, 1999).
27. Widmann, M. & Tett, S. F. B. Simulating the climate in the last millennium. *PAGES News* **11**(2&3), 21–23 (2003).
28. Mann, M. E. & Rutherford, S. Climate reconstruction using 'Pseudoproxies'. *Geophys. Res. Lett.* **29,** 1501, doi:10.1029/2001GL014554 (2002).
29. Zorita, E., González-Rouco, F. & Legutke, S. Testing the Mann *et al.* 1998 approach to paleoclimate reconstructions in the context of a 1000-yr control simulation with the ECHO-G coupled climate model. *J. Clim.* **16,** 1378–1390 (2003).
30. Stott, P. A. *et al.* External control of 20th century temperature by natural and anthropogenic forcings. *Science* **290,** 2133–2137 (2000).

Correspondence and requests for materials should be addressed to A.M. (anders.moberg@misu.su.se).